SnS$_2$/N-Doped Graphene as a Superior Stability Anode for Potassium-Ion Batteries by Inhibiting "Shuttle Effect"

Chuanchao Sheng[+],[a] Chaofei Zhang[+],[a] Xiaoxiao Shen,[a] Shulin Zhao,[a] Lijun Fu,[a] Yuping Wu,[a] Jing Wang,*[a] and Yuhui Chen*[a]

Potassium-ion batteries are promising supplements to lithium-ion batteries considering the abundance of potassium. However, the high reactivity of metallic potassium and low capacity of graphite anode are great challenges. A high capacity anode material is desired. Herein, we synthesize a tin sulfide/N-doped reduced graphene oxide composite (SnS$_2$/N-rGO), in which tin sulfide nanoparticles are dispersed on the N-doped graphene layer. It shows a high reversible capacity of 645.2 mAh g^{-1} at 50 mA g^{-1} and 402 mAh g^{-1} at 1 A g^{-1}. In situ X-ray powder diffraction of the discharge process is carried out. KSn forms as a final product and K$_2$S$_5$ forms as an important discharge intermediate. Nitrogen-doping immobilizes the tin sulfide particles and inhibits the loss of polysulfide intermediate. Therefore, 97.3% of discharge capacity remains after 100 cycles. This result sheds light on the rational design of anode materials with large volume change for potassium ion batteries.

Potassium ion battery attracts people's attention as a good supplement to Li-ion batteries and it owns some specific advantages, such as low cost and abundance.[1] Although K$^+$ is heavier than Li$^+$, K-ion battery might address the demands for some weight-less-dependent applications like the electric grid system.[2] K has a low potential close to Li, (100 mV vs Li) and it is approx. 220 mV lower potential than Na, allowing it to deliver a high working voltage and thus high power and specific energy.[3] However, the reactivity of metallic K anode is a great concern to safety and the low potential of K leads to the risk of dendrite formation during discharge-charge cycles.[4] Graphite anode in a K-ion battery shows a much lower capacity (278 mAh g^{-1})[5] than its capacity in a Li-ion battery (372 mAh g^{-1}).[6] Among other anode candidates, SnS$_2$ has a high theoretical capacity (733 mAh g^{-1}) due to the combination of the conversion process and alloying process of forming KSn.[7] However, its low conductivity and volume change during cycling restricts its capacity and cycling performance.

Due to the low conductivity of SnS$_2$, it is mixed with some carbon materials like graphene to form a SnS$_2$/C composite to improve the conductivity.[8] This kind of simply mixed composites did not solve the problems because SnS$_2$ particles aggregate during cycling.[9] As a result, the electrode material detaches from the current collector, and thus the capacity rapidly decreases.

Herein we synthesized the SnS$_2$/N-doped rGO composite as anode materials for K-ion batteries using a facile hydrothermal process. The SnS$_2$ nanoparticles were dispersed on the N-doped graphene layer like a lasagne. The graphene structure significantly improves its conductivity and mitigates the volume expansion on the discharge process. The N-doped graphene helps to immobilize the SnS$_2$ particles on the surface of graphene layers and prevent the aggregation of particles during cycling. Additionally, the polysulfide intermediate K$_2$S$_5$ escaped from the surface and remains during discharge and thus leads to a low coulombic efficiency and capacity decay. The N-doping appears to inhibit the shuttling effect of polysulfide species which are important intermediates in the discharging process. The SnS$_2$/N-rGO composite anode shows a reversible capacity of 645.2 mAh g$^{-1}_{SnS2}$ at 50 mA g$^{-1}_{SnS2}$ and 97.3% of the capacity remains after 100 cycles and a capacity of 335 mAh g$^{-1}_{SnS2}$ after 200 cycles at 1000 mAg^{-1}.

X-ray diffraction pattern (XRD) of the SnS$_2$/N-rGO sample was shown in Figure 1a. SnS$_2$/N-rGO composite has the same XRD patterns as SnS$_2$ nanoparticles (JCPDS card no. 23–0677). A small peak at 25.9° is assigned to rGO. SEM images (Figure 1b&c) shows that small SnS$_2$ particles (~5 nm) were evenly dispersed on the surface of graphene, which is consistent with the TEM image (Figure 1d). Facets (100) and (101) were identified in the TEM image (Figure 1e), which is in accordance with the XRD results. The facet (001) shifts slightly to the positive direction and it is consistent with literature,[10] which is probably due to the interaction SnS$_2$ and N-rGO substrate. EDS mapping of N, Sn, and S was carried out to confirm that N-doping and SnS$_2$ are evenly dispersed in the composite, as shown in Figure 1f. The N$_2$ adsorption-desorption isotherms are shown in Figure S1 and the BET surface area of SnS$_2$/N-rGO is 180.5 m^2/g, which provides large surface for the conversion reactions of SnS$_2$. Raman spectrum of SnS$_2$/N-rGO is shown in Figure S2. The ratio of D-band to G-band (I_D/I_G) of SnS$_2$/N-rGO is 1.38, higher than I_D/I_G of N-rGO (1.17). The formation of composite introduces more surface defects on the N-rGO, and thus immobilizes SnS$_2$ particles and inhibits the aggregation of nanoparticles.[11] To quantify the composition of SnS$_2$ in the

[a] C. Sheng,[+] C. Zhang,[+] X. Shen, Dr. S. Zhao, Prof. L. Fu, Prof. Y. Wu,
     Dr. J. Wang, Prof. Y. Chen
     State Key Laboratory of Materials-oriented Chemical Engineering,
     School of Energy Science and Engineering,
     Nanjing Tech University, Nanjing, Jiangsu, 211816 China
     E-mail: cheny@njtech.edu.cn
             wjx2015@njtech.edu.cn
[+] These authors contributed equally to this work.
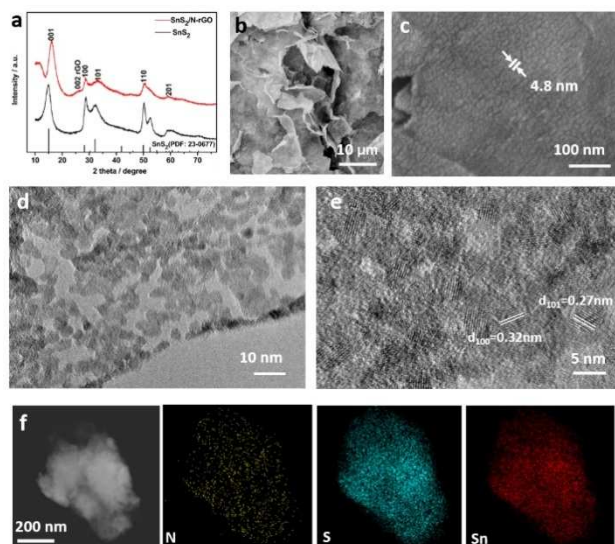
Figure 1. Characterization of SnS_2/N-rGO composite. (a) XRD patterns of SnS_2/N-rGO and SnS_2; (b,c) SEM image of SnS_2/N-rGO; (d,e) TEM images of SnS_2/N-rGO; (f) HAADF image and EDS maps of SnS_2/N-rGO.

composite, TGA was performed under air and 82.5 (wt%) of SnS_2 was contained in the composite, Figure S3.

To further understand the surface condition of SnS_2/N-rGO composite, XPS was carried out and spectra are shown in Figure 2. The survey spectra shows four main elements, Sn, S, C, and N in Figure 2a, which is consistent with the results of EDS in Figure 1f. In the N-spectrum, three types of N are identified, which are pyridinic N (398.7 eV), pyrrolic N (399.9 eV), and amino N (401.4 eV). The pyridinic-N and pyrrolic-N introduce numerous active sites and extrinsic defects to graphene, thereby improving the electrochemical performance, consistent with previous results. The C 1s spectrum (Figure 2c) of SnS_2/N-rGO shows four peaks and they are assigned to C—C (284.6 eV),
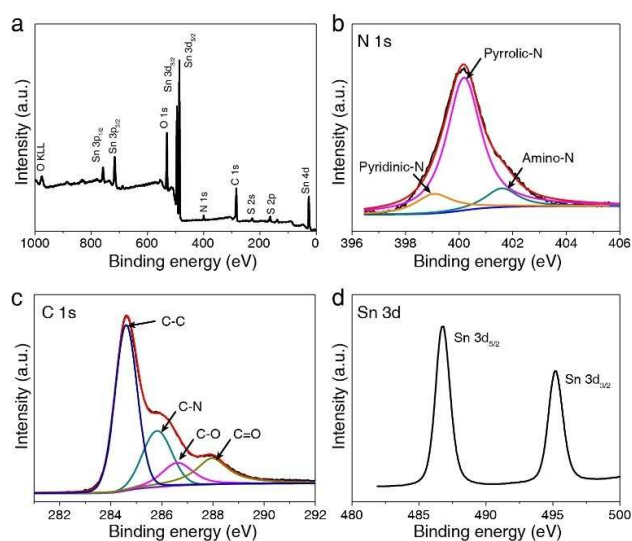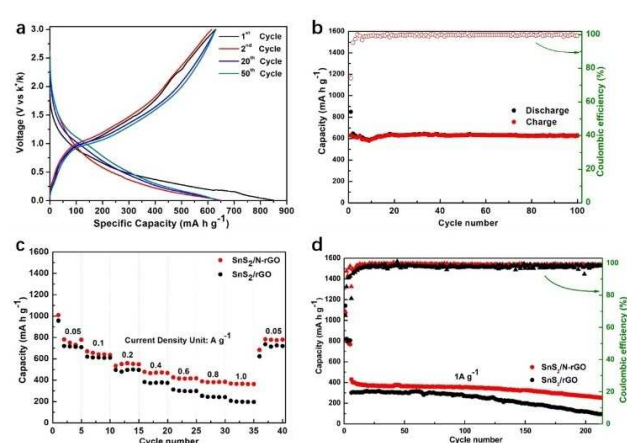
C—N (285.6 eV), C—O(286.6 eV), and O—C≡O(288.0 eV). The S 2p spectra of SnS_2/N-rGO and SnS_2 are shown in Figure S4. The peak at 186.5 eV assigned to S-doping on rGO does not appear.[12] The Sn 3d spectrum in Figure 2d shows two peaks with binding energy at 487.0 and 495.4 eV, assigned to the Sn $3d_{5/2}$ and Sn $3d_{3/2}$ respectively, confirm the presence of Sn^{4+} in this composite.[13]

The electrochemical performance of the SnS_2/N-rGO composite was tested in a coin cell. The electrode fabrication process was described in the Experimental section. The load curves for discharge and charge were shown in Figure 3a. Two stages were observed on discharge. The first stage is a slope from 1.2 V to 0.5 V and the second stage is from 0.5 V to 0.01 V. These two discharge stages are clearly exhibited in the dQ/dV plot in Figure S5a and this result is consistent with the CV results in Figure S5b. To understand the discharge process, in-situ XRD was carried out and the results were shown in Figure 4. The Schematics of the in-situ XRD cell shows in Figure S6. All XRD results are subtracted with the pristine one to exhibit the change clearly. The negative peak at 17° and 27° is due to the consumption of SnS_2. XRD patterns distinctly exhibit two stages of discharge process. At stage I (2.5∼0.5 V, shadow region in Figure 4), SnS_2 is consumed while K_2S_5 and SnS are formed, suggesting the conversion reaction of SnS_2 to form SnS and K_2S_5 [Eq. (1)].

$$5SnS_2 + 2K^+ + 2e^- \rightleftharpoons K_2S_5 + 5SnS \qquad (1)$$
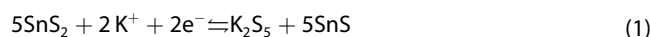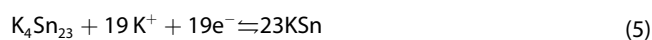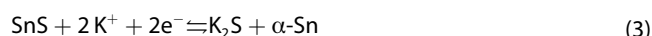
At stage II (0.5∼0.01 V), the peak of SnS gradually disappears, while the peaks assigned to α-Sn and K_2S increase. K_2S_5 is reduced to K_2S [Eq. (2)]. SnS is further reduced to α-Sn [Eq. (3)] following the alloying reactions of Sn and K [Eq. (4)–(5)]. As shown in Figure 4a, K_4Sn_{23} was identified as an intermediate and its peaks grow and then disappear while approaching to the end of discharge. Eventually, KSn was formed as the final product [Eq. (5)].

Figure 2. XPS spectra of SnS_2/N-rGO composite. (a) Full spectrum; (b) N; (c) C and (d) Sn spectra of SnS_2/N-rGO composite.

Figure 3. Electrochemical performance of SnS_2/N-rGO composite. (a) Charge-discharge profiles of 1st, 2nd, 20th and 50th cycles at a current density of 50 mA g^{-1} for SnS_2/N-rGO. (b) Capacity retention and coulombic efficiency during cycling of SnS_2/N-rGO. Current density: 50 mA g^{-1} (c) Rate capability of the SnS_2/N-rGO and SnS_2/rGO from 0.05 A g^{-1} to 1 A g^{-1}. (d) The cycling performance of SnS_2/N-rGO, SnS_2/rGO at a current density of 1 A g^{-1}.
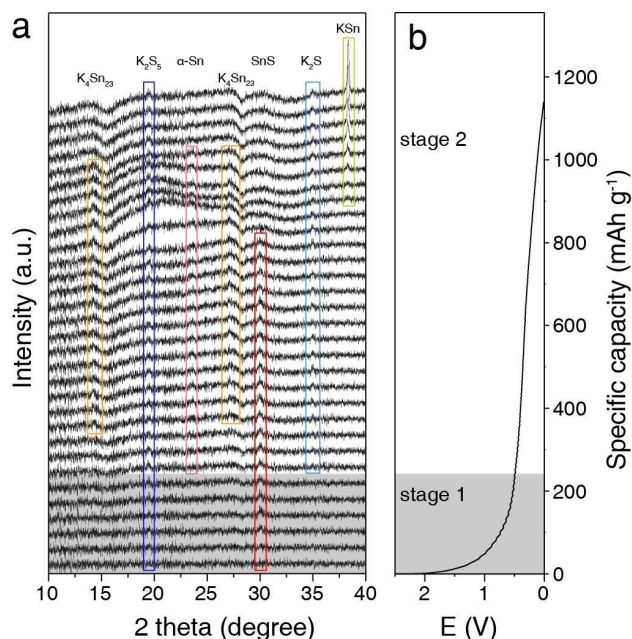
Figure 4. In situ XRD patterns of the SnS$_2$/N-rGO composite electrode during discharge. (a) XRD patterns and (b) corresponding discharge load curve.

$$K_2S_5 + 8\,K^+ + 8e^- \rightleftharpoons 5\,K_2S \tag{2}$$

$$SnS + 2\,K^+ + 2e^- \rightleftharpoons K_2S + \alpha\text{-}Sn \tag{3}$$

$$23\,Sn + 4\,K^+ + 4e^- \rightleftharpoons K_4Sn_{23} \tag{4}$$

$$K_4Sn_{23} + 19\,K^+ + 19e^- \rightleftharpoons 23\,KSn \tag{5}$$

Interestingly, unlike other intermediates such as SnS, α-Sn, and K$_4$Sn$_{23}$, the signal of K$_2$S$_5$ did not fully disappear at the end of discharge, which suggests an incomplete conversion of K$_2$S$_5$ to K$_2$S [Eq. (2)]. It could be due to the sluggish kinetics of further reduction of K$_2$S$_5$ and its nonnegligible solubility in the electrolyte. The images of the separators after 100 cycles for SnS$_2$/rGO electrodes was shown in Figure S7a. We found that the separator exhibited a yellowish color, similar to situation in a Li–S battery. For analysis, the residue at the separator was rinsed with 2 ml of EC/DEC mixture solvent and the UV-vis spectrum of the latter was recorded in Figure S8. Two absorbance bands at 360 nm and 430 nm, assigned to S$_6^{2-}$ and S$_4^{2-}$,[14] are identified in the separator for SnS$_2$/rGO. The UV-vis result is consistent with the formation of polysulfide K$_2$S$_5$ and polysulfide diffuses away from electrode surface, leading to a capacity decay during cycling. The N-doping at cathode could help to immobilize the polysulfide and inhabit its shuttling. The separator of SnS$_2$/N-rGO shows little yellowish color in Figure S7b. Dissolved S$_6^{2-}$ and S$_4^{2-}$ intermediates are not identified in the sample from SnS$_2$/N-rGO because of the strong interaction between N-doping and polysulfide. The XPS spectra of the composite electrodes after 100 cycles were collected and shown in Figure S9. The band of SnS$_2$ disappears at very outer surface of SnS$_2$/rGO electrode after cycling, indicating that the SnS$_2$ at the outer surface is consumed during the discharge/

charge cycling. In contrast, the band of SnS$_2$ at SnS$_2$/N-rGO electrode remains. The N-doping could effectively immobilize polysulfide and enhance capacity retention and cyclability, as same as the strategy in Li–S batteries.[15]

On the following charge process, two oxidation peaks appear at 1 V and at 1.7 to 2.3 V, Figure 3a, which are assigned to the depotassiation process of KSn alloy and K$_2$S. This result is consistent with the CV curve of the charging process in Figure S5b. Since the 2nd cycle, both galvanostatic curves and CV curves of the following cycles become identical, suggesting good reversibility and cyclability of the cell after initial activation. Figure 3b exhibits the cycling profile and capacity retention of cycling of SnS$_2$/N-rGO. For SnS$_2$/N-rGO, the initial discharge capacity is 848.7 mAh g^{-1}, slightly higher than theoretical capacity due to some side-reactions, i.e. SEI formation. The capacity decreased to 645.2 mAh g^{-1} after a short activation process and it remains at 630 mAh g^{-1} after 100 cycles. This capacity is about 86% of the theoretical capacity (733 mAh g^{-1}). It shows no significant capacity decay after 100 cycles. After the SEI formation at the first cycle, the capacity retention from the 2nd to 100th cycles is 97.3%. As shown in Figure S10, the capacity of N-rGO itself is less than 30 mAh/g and it is inert for K$^+$ storage, therefore the capacity in the SnS$_2$/N-rGO is mainly contributed by SnS$_2$. However, the pristine SnS$_2$ electrode shows a poor cyclability as shown in Figure S11. Its initial capacity is 320.9 mAh g^{-1} and it rapidly reduces to 50 mAh g^{-1} after 10 cycles. When SnS$_2$ is coupled with rGO, the discharge capacity increases to 842.9 mAh g^{-1} in Figure S12. RGO improves the conductivity of the composite and it also separates SnS$_2$ particles and thus inhibits the aggregation of SnS$_2$ particles to some extent but not completely. However, the capacity decays steadily and the capacity is below 400 mAh g^{-1} after 50 cycles. The capacity decay is attributed to aggregation of SnS$_2$ particles and dissolution of polysulfide. This comparison between SnS$_2$/rGO and SnS$_2$/N-rGO distinctly confirms the effect of N-doping on improving the capacity and cyclability by immobilizing SnS$_2$ particles and polysulfide intermediate at cathode. EIS results before and after 20 cycles are consistent with the effect, Figure S13. Their initial impedance spectra before cycling are similar. After 20 cycles, the impedance of SnS$_2$/N-rGO is much smaller than the rest. TEM images of the SnS$_2$/N-rGO and SnS$_2$/rGO electrodes after 100 cycles are shown in Figure S14. The SnS$_2$ remains small nanoparticles dispersed on the N-doped graphene layer for SnS$_2$/N-rGO, however, the aggregation of particles happens for SnS$_2$/rGO after cycling.

The well-dispersed SnS$_2$ morphology also resulted in good rate capability. The electrochemical performance at various current was carried out, Figure 3c. SnS$_2$/N-rGO delivered a higher capacity than SnS$_2$/rGO. For SnS$_2$/N-rGO from 0.05 to 1.0 A g^{-1}, remaining 729.1 mAh g^{-1} to 365.5 mAh g^{-1}. When the current density returns to 50 mA g^{-1}, the capacity increases to approx. 800 mAh g^{-1} close to the initial capacity exhibiting an impressive rate capability. At a high current density of 1 A g^{-1} (approx. 1.36 C), the capacity of SnS$_2$/N-rGO is 402 mAh g^{-1}, approx. 2-fold than that of SnS$_2$/rGO (200 mAh g^{-1}). The good rate capacity is attributed to the improved conductivity of SnS$_2$/N-rGO, and the suppression of escape of polysulfides. By

dispersing SnS$_2$ nanoparticles evenly between N-rGO layers, electron can be easily passed on to the SnS$_2$ from graphene layers and the conductivity of the composite is improved. For high rate cycling at a current density of 1 A g^{-1}, SnS$_2$/N-rGO shows a capacity 355 mAh g^{-1} after 200 cycles, Figure 3d.

In summary, we synthesized the SnS$_2$/N-rGO composite for the anode materials for a K-ion battery using a facile hydrothermal method. The N-rGO improves the conductivity of the composite and N-doping immobilizes the SnS$_2$ particles and polysulfide intermediate on the rGO and thus successfully inhibits the consequence of the volume change and capacity decay. SnS$_2$/N-rGO composite shows a high reversible capacity of 645.2 mAh g^{-1}$_{SnS2}$ at 50 mA g^{-1} and 402 mAh g^{-1}$_{SnS2}$ at 1 A g^{-1}. In situ XRD shows that KSn forms as a final product and the soluble polysulfide intermediate might be the species that restrict the electrochemical performance. N-doping graphene might effectively alleviate the polysulfide shuttling effect and reduces the charge-transfer resistance thus it has a high capacity, superior high-rate capability, and long term cycling stability. This strategy allows people to improve and optimize the design of anode materials based on conversion and alloying reaction, which owns high capacity but low conductivity or high volume change during cycling.

Acknowledgments

Conflict of Interest

The authors declare no conflict of interest.

[1] a) T. Li, Q. Zhang, *J. Energy Chem.* **2018**, *27*, 373–374. b) H. Gao, T. Zhou, Y. Zheng, Q. Zhang, Y. Liu, J. Chen, H. Liu, Z. Guo, *Adv. Funct. Mater.* **2017**, *27*, 1702634. c) K. S. Huang, Z. Xing, L. C. Wang, X. Wu, W. Zhao, X. J. Qi, H. Wang, Z. C. Ju, *J. Mater. Chem. A* **2018**, *6*, 434–442. d) X. P. Wang, X. M. Xu, C. J. Niu, J. S. Meng, M. Huang, X. Liu, Z. Liu, L. Q. Mai, *Nano Lett.* **2016**, *17*, 544–550.

[2] a) Y. Hironaka, K. Kubota, S. Komaba, *Chem. Commun.* **2017**, *53*, 3693–3696. b) S. Komaba, T. Hasegawa, M. Dahbi, K. Kubota, *Electrochem. Commun.* **2015**, *60*, 172–175. c) I. Sultana, M. M. Rahman, Y. Chen, A. M. Glushenkov, *Adv. Funct. Mater.* **2018**, *28*, 1703857. d) J. Y. Hwang, S. T. Myung, Y. K. Sun, *Adv. Funct. Mater.* **2018**, *28*, 1802938.

[3] a) W. C. Zhang, J. F. Mao, S. A. Li, Z. X. Chen, Z. P. Guo, *J. Am. Chem. Soc.* **2017**, *139*, 3316–3319. b) Z. L. Jian, W. Luo, X. L. Ji, *J. Am. Chem. Soc.* **2015**, *137*, 11566–11569. c) J. C. Pramudita, D. Sehrawat, D. Goonetilleke, N. Sharma, *Adv. Energy Mater.* **2017**, *7*, 1602911.

[4] a) N. Xiao, W. D. McCulloch, Y. Y. Wu, *J. Am. Chem. Soc.* **2017**, *139*, 9475–9478. b) H. Fei, Y. Liu, Y. An, X. Xu, G. Zeng, Y. Tian, L. Ci, B. Xi, S. Xiong, J. Feng, *J. Power Sources* **2018**, *399*, 294–298.

[5] a) W. Luo, J. Y. Wan, B. Ozdemir, W. Z. Bao, Y. N. Chen, J. Q. Dai, H. Lin, Y. Xu, F. Gu, V. Barone, L. B. Hu, *Nano Lett.* **2015**, *15*, 7671–7677. b) Y. Liu, F. F. Fan, J. W. Wang, Y. Liu, H. L. Chen, K. L. Jungjohann, Y. H. Xu, Y. J. Zhu, D. Bigio, T. Zhu, C. S. Wang, *Nano Lett.* **2014**, *14*, 3445–3452.

[6] a) T. Ohzuku, Y. Lwakoshi, K. Sawai, *J. Electrochem. Soc.* **1993**, *140*, 2490–2498.

[7] a) T. Ramireddy, R. Kali, M. K. Jangid, V. Srihari, H. K. Poswal, A. Mukhopadhyay, *J. Electrochem. Soc.* **2017**, *164*, 2360–2367. b) Q. N. Wang, X. X. Zhao, C. L. Ni, H. Tian, J. X. Li, Z. Zhang, S. X. Mao, J. W. Wang, Y. H. Xu, *J. Phys. Chem. C* **2017**, *121*, 12652–12657. c) D. S. Bin, S. Y. Duan, X. J. Lin, L. Liu, Y. Liu, Y. S. Xu, Y. G. Sun, X. S. Tao, A. M. Cao, L. J. Wan, *Nano Energy* **2019**, *60*, 912–918.

[8] a) V. Lakshmi, Y. Chen, A. A. Mikhaylov, A. G. Medvedev, I. Sultana, M. M. Rahman, O. Lev, P. V. Prikhodchenko, A. M. Glushenkov, *Chem. Commun.* **2017**, *53*, 8272–8275. b) Y. Jiang, M. Wei, J. Feng, Y. Ma, S. Xiong, *Energy Environ. Sci.* **2016**, *9*, 1430–1438. c) B. H. Qu, C. Z. Ma, G. Ji, C. H. Xu, J. Xu, Y. S. Meng, T. H. Wang, J. Y. Lee, *Adv. Mater.* **2014**, *26*, 3854–3859. d) C. Zhu, X. Mu, P. A. van Aken, Y. Yu, J. Maier, *Angew. Chem. Int. Ed.* **2014**, *53*, 2152–2156. e) J. Wang, C. Luo, T. Gao, A. Langrock, A. C. Mignerey, C. Wang, *Small* **2015**, *11*, 473–481. f) Z. C. Liu, X. H. Yuan, S. S. Zhang, J. Wang, Q. H. Huang, N. F. Yu, Y. S. Zhu, L. J. Fu, F. X. Wang, Y. H. Chen, Y. P. Wu, *NPG Asia Mater.* **2019**, *11*, 12.

[9] a) X. Yang, L. Zhang, F. Zhang, Y. Huang, Y. S. Chen, *ACS Nano* **2014**, *8*, 5208–5215. b) Z. Wang, Y. Dong, H. Li, Z. Zhao, H. B. Wu, C. Hao, S. Liu, J. Qiu, X. W. Lou, *Nat. Commun.* **2014**, *5*, 5002. c) X. Zhou, L. J. Wan, Y. G. Guo, *Adv. Mater.* **2013**, *25*, 2152–2157.

[10] B. Luo, Y. Fang, B. Wang, J. S. Zhou, H. H. Song, L. J. Zhi, *Energy Environ. Sci.* **2012**, *5*, 5226–5230.

[11] a) K. Share, A. P. Cohn, R. Carter, B. Rogers, C. L. Pint, *ACS Nano* **2016**, *10*, 9738–9744. b) C. Chen, Z. Wang, B. Zhang, L. Miao, J. Cai, L. Peng, Y. Huang, J. Jiang, Y. Huang, L. Zhang, J. Xie, *Energy Storage Mater.* **2017**, *8*, 161–168. c) Z. Li, Q. He, X. Xu, Y. Zhao, X. Liu, C. Zhou, D. Ai, L. Xia, L. Mai, *Adv. Mater.* **2018**, *30*, 1804089.

[12] a) W. Shen, C. Wang, Q. Xu, H. Liu, Y. Wang, *Adv. Energy Mater.* **2015**, *5*, 1400982. b) W. Luo, F. Li, J.-J. Gaumet, P. Magri, S. Diliberto, L. Zhou, L. Mai, *Adv. Energy Mater.* **2018**, *8*, 1703237. c) J. Bai, B. Xi, H. Mao, Y. Lin, X. Ma, J. Feng, S. Xiong, *Adv. Mater.* **2018**, *30*, 1802310. d) G. Zhou, E. Paek, G. S. Hwang, A. Manthiram, *Nat. Commun.* **2015**, *6*, 7760.

[13] a) H. Hu, Z. B. Zhao, W. B. Wan, Y. Gogotsi, J. S. Qiu, *Adv. Mater.* **2013**, *25*, 2219–2223. b) Y. Zhang, P. Zhu, L. Huang, J. Xie, S. Zhang, G. Cao, X. Zhao, *Adv. Funct. Mater.* **2015**, *25*, 481–489.

[14] G. Bieker, J. Wellmann, M. Kolek, K. Jalkanen, M. Winter, P. Bieker, *Phys. Chem. Chem. Phys.* **2017**, *19*, 11152–11162.

[15] a) X. Lu, M. E. Bowden, V. L. Sprenkle, J. Liu, *Adv. Mater.* **2015**, *27*, 5915–5922. b) Q. Zhao, Y. Hu, K. Zhang, J. Chen, *Inorg. Chem.* **2014**, *53*, 9000–9005. c) Q. Zou, Z. Liang, G. Y. Du, C. Y. Liu, E. Y. Li, Y. C. Lu, *J. Am. Chem. Soc.* **2018**, *140*, 10740–10748. d) S. S. Zhang, *J. Power Sources* **2013**, *231*, 153–162.